Preparation and oxygen-evolution-reaction performance of sulphur-doped flower-like NiFe-based composites supported on biomass porous carbon

Q. Lou, S. Zhong, T. Li*, S. Ling

School of Mechanical Engineering, Chengdu University, Chengdu, 610106, Sichuan, China

Hydrogen gas generated through water electrolysis can replace fossil fuels. Thus, developing cost-effective and efficient water-splitting electrocatalysts for oxygen evolution reaction is highly important. Herein, biomass-porous-carbon-supported sulphur-doped flower-like NiFe-based alloy composites are prepared using an *in situ* impregnation–heat treatment technology. The spherical flower (diameter ≈ 1 μm, petal thickness ≈ 20 nm) main components are $Ni_{0.5}Fe_{0.5}$ and $Fe_9Ni_9S_{16}$. The 800 °C heat-treated catalyst demonstrates outstanding catalytic performance in oxygen evolution reactions. At a current density of 10 mA cm^{-2}, it exhibits a minimal overpotential of 298.62 mV.

(Received February 13, 2024; Accepted May 3, 2024)

Keywords: Biomass porous carbon, Sulphur doping, NiFe, Oxygen evolution reaction, Synergistic effect

1. Introduction

Hydrogen, a renewable and eco-friendly energy source. It has several advantages such as no environmental pollution and zero emissions. By 2024, the global demand for hydrogen will increase to 120 million tons. Currently, one of the most promising technologies for hydrogen production is water electrolysis, which achieves high-purity hydrogen without generating by-products. However, this technology is inefficient, producing less than 5% of the world's total hydrogen production.[1-3]. One of the main factors affecting the efficiency of hydroelectrolysis is the high overpotential and dynamics barriers in the oxygen evolution reaction (OER)[4,5], which involves multiple proton–electron coupling on the anode surface. Therefore, developing OER catalysts that can reduce the overpotential and enhance the water electrolysis efficiency is a highly challenging task[6]. Although catalysts based on noble metals like ruthenium and iridium show high catalytic efficiency, they are costly and have poor stability.[7], limiting their large-scale applications. Therefore, currently, developing cost-effective and efficient catalysts for hydrogen production have become a research focus.

Catalysts based on transition metals, including iron, cobalt, nickel, and manganese compounds, demonstrate notable activity for OER process in environments with alkaline electrolytes. Thus, they are considered excellent alternatives to precious metal-based catalysts[7,8]. The electronic structures of bimetallic composite OER catalysts can be altered and a synergistic effect can be induced between the different metal atoms within the catalyst by changing the element types and their atomic ratios[9]. This considerably enhances the conductivity during OER and improves the composite catalytic efficiency. Among bimetallic composites, NiFe alloy composite materials are among the most active catalysts in alkaline electrolytes[10,11]. Employing a chemical bath deposition technique reliant on a solution, the research team led by Ahmed applied exceedingly clear iron-nickel hydroxide OER catalysts onto conductive glass bases (fluorine-doped tin oxide). These catalysts demonstrated a 290 mV overpotential necessary to produce a current density of 10 mA cm^{-2} within a NaOH alkaline electrolyte (1.0 mol L^{-1}).

* Corresponding author: litao@cdu.edu.cn
https://doi.org/10.15251/DJNB.2024.192.693

The superior catalytic activity was attributed to the Ni/Fe alloys, which reduced the surface adsorption resistance of the intermediates during the catalytic process [12]. Doping with a non-metal anion compound strategy can further increase the catalytic activity, stability and specific surface area of the catalyst [13].The Huiying Kang research group prepared CoFe-Layered double hydroxides precursor using a single-nucleation-and-ageing-step method. The precursor was subjected to sulfidation, selenisation, annealing heat treatment and other steps to obtain a solid solution of Co0.75Fe0.25(S0.2Se0.8)2. Electrochemical tests in alkaline media showed that the overpotential was 293 mV (10 mA cm-2), indicating better electrocatalytic performance than the control group with only sulfurization or selenization [13].

The use of multi-element alloys and doping strategies can improve catalytic activity to a certain extent, while reducing the overpotential of the catalyst; however, they do not address the agglomeration and poor stability problems[14]. In 2009, scientists first discovered that carbon-based electrocatalysts derived from N-doped carbon nanotubes demonstrate activity for catalyzing the oxygen reduction process. Thus, researchers successfully combined transition metal compounds with carbon materials to obtain an efficient catalyst[15-18]. However, the preparation process of carbon materials, such as GE and CNTs, is complex and costly, hindering their use in large-scale applications.

In this study, agricultural waste (sorghum husk) was used as raw material to prepare biomass carbon with a three-dimensional porous structure. Using biomass carbon as a carrier, biomass porous carbon-supported sulphur-doped flower-like NiFe-based mixed crystal composite catalysts were prepared using an *in situ* technology involving metal salt ion impregnation and heat treatment. The basic properties and electrochemical performance of NiFe-based mixed crystal composite catalysts were thoroughly investigated. This research lays the groundwork for devising water-splitting OER catalysts that are both effective and economical to produce.

2. Experimental

2.1. Raw materials

Sorghum husk (agricultural by-products), heptahydrate ferrous sulphate ($FeSO_4$ $7H_2O$, 99.0%), nickel acetate ($Ni(CH_3COO)_2$ $4H_2O$, 98.5%), deionised water (synthesized by a laboratory reverse osmosis ultrapure water machine), potassium hydroxide (KOH, 85.0%), anhydrous ethanol (CH_3CH_2OH, 97%), nafion solution (5%), high-purity argon gas (99.99%) and conductive carbon paper (0.5 cm × 0.5 cm) was used in the composite preparation. All reagents were of analytical grade.

2.2. Experimental instruments

A small tubular furnace (KMTF.1100-S-50-220), an ultrasonic cleaning machine (VGT-1990QTD), a precision electric heating blast drying oven (TST202A-00), an electrochemical workstation (CS350M), a sealed electrolytic cell (100 mL) as well as several glassware were used in the experiments.

2.3. Sample preparation

The Ni/Fe–S/C catalyst was prepared using an *in situ* impregnation–heat treatment method. The preparation process flow chart is shown in Fig. 1. Dry sorghum husk (10 g) was first soaked in deionised water (500 ml) at 25°C temperature for 24 h. The solution was subjected to ultrasonic treatment for 10 min every 8 h, and the deionised water was changed once. Clean sorghum husk was dried at 80 °C for 12 h and was then pulverized and filtered using a 100-mesh screen to obtain sorghum husk powder for later use.

Next, $Ni(CH_3COO)_2.4H_2O$ (3.98 g) and $FeSO_4.7H_2O$ (4.45 g) were added into ethanol solution (50%, 80 ml) to form a solution with a total ion concentration of 0.4 mol L^{-1} and a molar ratio of nickel to iron ions (n_{Ni}^{2+}: n_{Fe}^{2+}) of 1:1. Sorghum husk powder (8 g) was then added to the mixture. Under sealed conditions, the mixed solution was heated at 60°C for 1.5 hours in a water bath. Subsequently, filter and dry at 60 ° C for 3 hours to obtain the precursor. The sorghum husk precursor was divided into an average of seven parts (1.14 g per serving) and subjected to heat

treatment at 400 °C, 500 °C, 600 °C, 700 °C, 800 °C, 900 °C and 1,000 °C, respectively, under an argon atmosphere. The experimental samples corresponding to these temperatures were labelled S-400, S-500, S-600, S-700, S-800, S-900 and S-1000, individually.

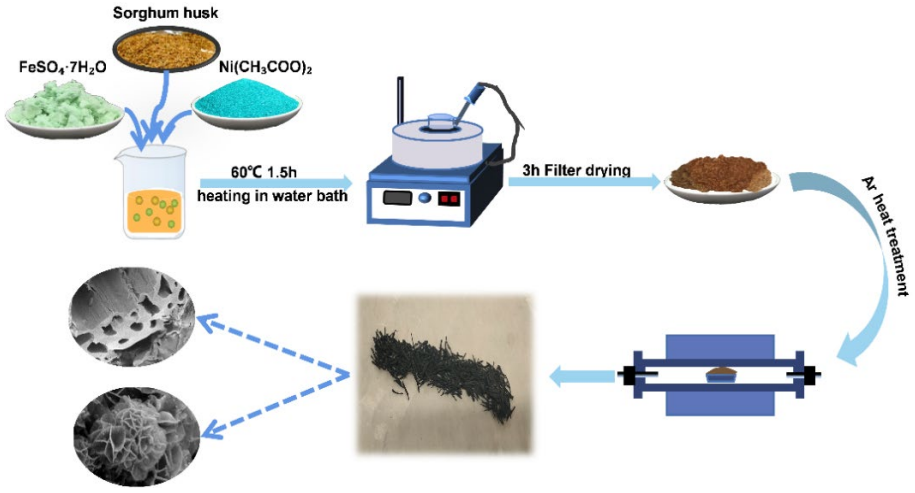

Fig. 1. The process of sample preparation.

2.4. Electrochemical performance testing and calculation

All electrochemical tests are performed at room temperature (25℃) using an electrochemical workstation. The counter electrode was platinum wire (0.5 mm×37 mm) , the reference electrode was Hg/HgO. The electrolyte is 1mol L^{-1} potassium hydroxide solution with pH=14.

Preparation of catalyst ink: deionised water (600 μL), ethanol (200 μL), nafion solution (5%, 30 μL) and the ground sample (5 mg) were mixed and ultrasonically dispersed for 30 min. Preparation of catalyst working electrode: The catalyst ink (20 μL) was dropped onto a conductive carbon paper and dried using an infra-red lamp.

Linear sweep voltammetry (LSV) has a test range of 0.0 - 1.0 V. Cyclic voltammetry (CV) was performed at scan rates of 0.02, 0.04, 0.06, 0.08, 0.08, and 0.1 V s^{-1}. At a potential of 0.05 V, the difference in current density shown on the CV curve is considered as an absolute value, which is then associated with the scan rate. The slope of the resulting straight line represents the specific capacitance (Cdl*, mF cm^{-2}). The equation (1) defines the double-layer capacitance Cdl, where 's' represents the electrode area. Equation (2) is utilized to compute the Electrochemical Active Surface Area (ECSA). In this formula, Cs represents the specific capacitance of the nickel-based catalyst on the unit electrochemical active area of the KOH electrolyte (mF cm^{-2}). The value of Cs in alkaline solutions is 0.022–0.130 mF cm^{-2} (typically, 0.04 mF cm^{-2})[19,20]. In addition, all reversible hydrogen electrode potentials of the polarisation curves were corrected based on the standard electrode potential, as shown in Equation (3)[21,22]. Electrochemical impedance spectroscopy (EIS) are tested at a potential of 0.6V, within a frequency range from 10^{-1} to 10^{5} Hz. The stability test curves (i-t) are obtained by conducting measurements for 12 hours at 0.6 V.

$$\mathrm{Cdl} = Cdl^{*} \times \mathrm{s} \tag{1}$$

$$\mathrm{ECSA} = \mathrm{Cdl} \div \mathrm{Cs} \tag{2}$$

$$E_{RHE}=E_{Hg/HgO} + 0.059\mathrm{pH} + 0.098 \tag{3}$$

2.5. Characterisation

The sample's phase composition were tested using XRD (DX-2700B). The morphology was characterised using SEM (Zeiss Sigma 300), and the elemental composition and content of the materials were analysed using EDS. The surface chemical states of the elements in the samples were determined using XPS (Thermo Scientific K-Alpha) equipped with Al Kα radiation (hv = 1,486.6 eV). The specific surface area and pore structure were analysed by a nitrogen adsorption and desorption instrument (V-Sorb 2800P). The structural characteristics of graphitisation of the samples were characterised using laser Raman spectroscopy (Invia, Renishaw, 514.5-nm laser).

3. Results and discussions

3.1. Morphology and structure characterisation

Figs. 2(a–d) show the SEM images of the sorghum husk samples S-sorghum husk-400, -600, -800 and -1000. The images reveal that the sorghum husk develops an excellent porous structure with various types of pores such as pores with grooved, circular, flat and irregular shapes. These pores form a hierarchical, composite and three-dimensional pore structures with different sizes, mainly in the micrometre range. This pore structure enhances the penetration and adsorption of metal salt solutions into the sorghum husk. Moreover, it allows the bubbles generated during the catalytic reaction to easily escape from the pores, improving the mass and heat transfer between the gas and liquid phases.

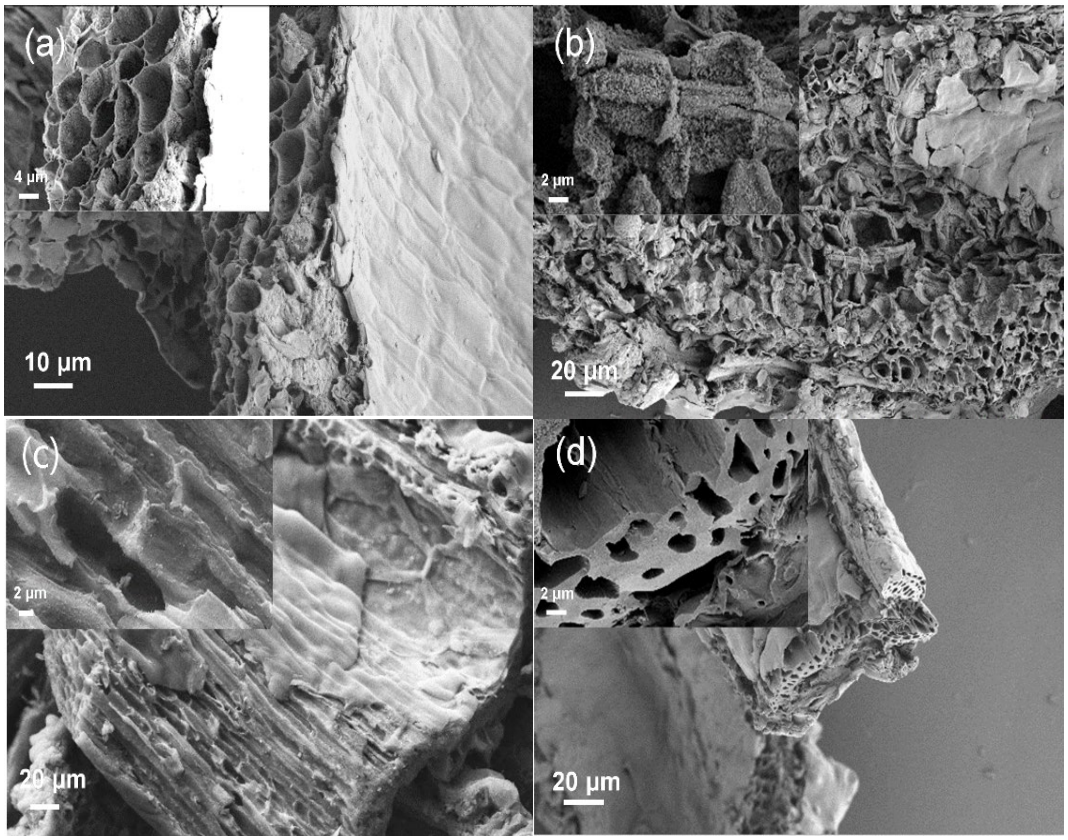

Fig. 2. SEM images of the heat-treated sorghum husk samples S-sorghum husk- (a) 400, (b) 600, (c) 800 and (d) 1,000.

The samples, i.e. S-500, S-600, S-700, S-800, S-900 and S-1000, were obtained by impregnating the carrier, i.e. sorghum husk, with iron and nickel salts and then heat treating it at

different temperatures. Figs. 3 (a–f) show the SEM results for these samples. The images indicate that the sorghum husk preserved its porous structure after the heat treatment, and flower-like alloy nanoparticles were attached to the pores. The alloy particles underwent different processes at different temperatures, resulting in different morphologies and sizes. At 500 °C [Fig. 3(a)], flower-like alloy particles (diameter ≈ 200 nm) started to grow and were anchored on the surface of the channel in a sparse and dispersed manner. At 600 °C [Fig. 3(b)], the flower-like alloy particles grew to a diameter of 500 nm and were anchored inside the channel. At 700 °C [Fig. 3(c)], dense and disordered nanosheet-like alloys formed in the channel. At 800 °C [Fig. 3(d)], flower-like alloy particles acted as growth seeds and further aggregated in the channel, forming spherical sheet-like petals of the NiFe alloy (size = 1 μm). At 900 °C [Fig. 3(e)], numerous alloy particles agglomerated owing to the increase in temperature, exhibiting two forms: spherical particles (diameter = 50 nm) and whole petals, which were evenly dispersed. At 1,000 °C [Fig. 3(f)], all nickel–iron alloys agglomerated to form larger alloy particles (particle size = 200–400 nm). Moreover, owing to the high temperature, the the material skeleton was severely carbonised forming a uniform porous structure (size = 200 nm) in which the alloy particles were embedded. The mapping in Fig. 4 indicates that the C, S, Ni, and Fe elements were homogeneously distributed within the biomass carbon material.

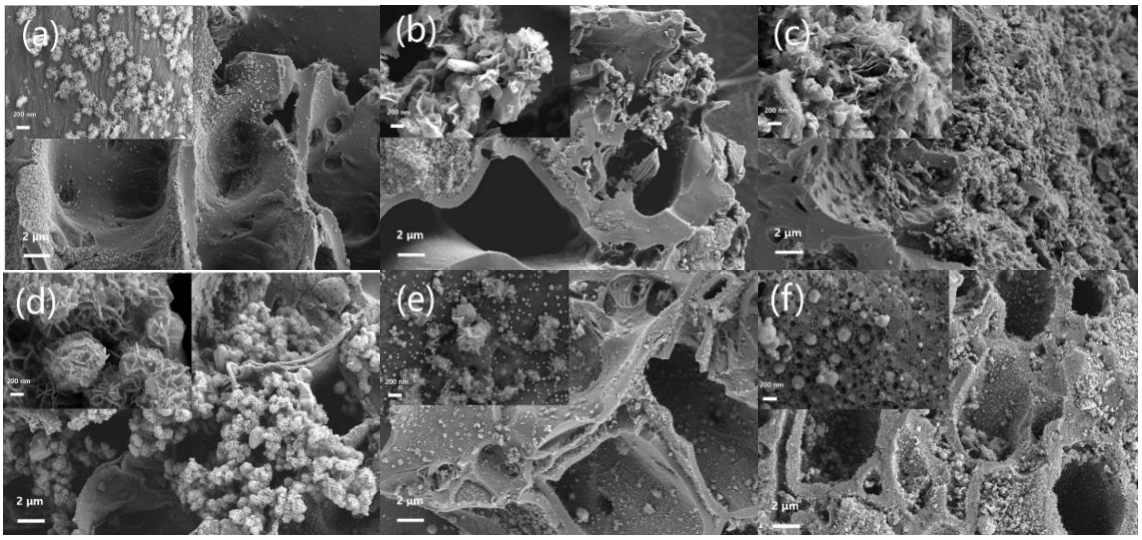

Fig. 3. SEM images of the catalysts heat-treated: (a) S-500, (b) S-600, (c) S-700 d S-800, (e) S-900 and (f) S-1000.

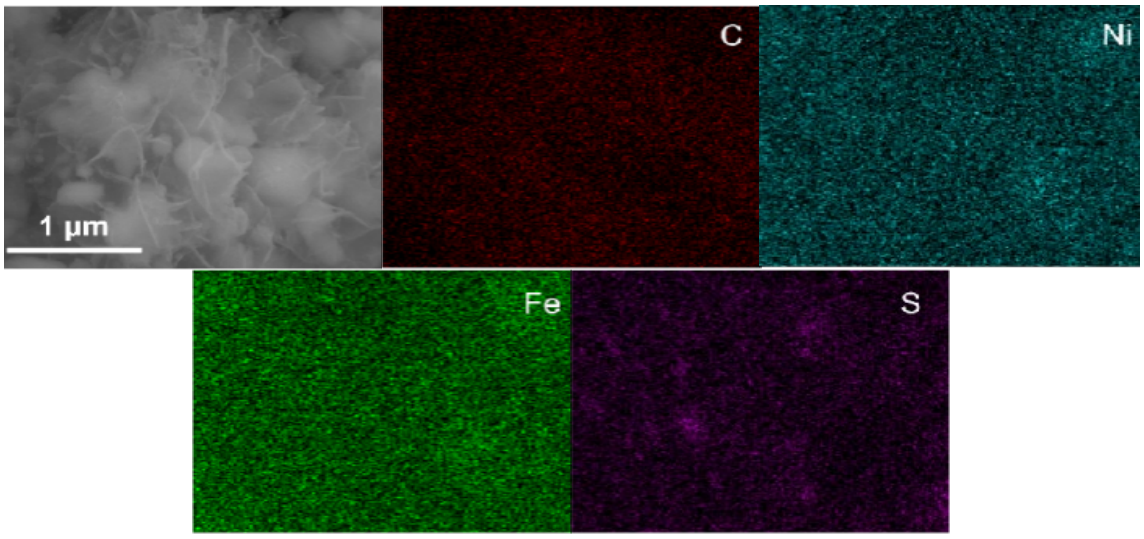

Fig. 4. Elemental mappings of Ni, Fe, S and C.

Figs. 5 (a and b) shows the results of the porous properties of samples. Fig. 5a shows that all curves exhibit type IV isotherms, with a sharp rise in nitrogen adsorption at low pressure and without hysteresis loop, signifying the existence of micropores within the samples [23,24]. A noticeable H4-type hysteresis loop is observed at P/P_0 = 0.4–1.0 for all samples, indicating the formation of layered slit pores [25]. The order of the sample's adsorption capacity was as follows: S-800 (169.64 mL g^{-1}) > S-900 (154.47 mL g^{-1}) > S-600 (143.18 mL g^{-1}) > S-700 (142.42 mL g^{-1}). The specific surface area of the samples was in the following order: S-800(282.89 m^2 g^{-1}) > S-600 (269.36 m^2 g^{-1}) > S-700 (264.50 m^2 g^{-1}) > S-900 (257.38 m^2 g^{-1}). With the increase in temperature, both the adsorption capacity (169.64 mL g^{-1}) and the specific surface area (282.89 m^2 g^{-1}) of S-800 reach their maximum values.

The average pore diameter of the samples is presented in Fig. 5b, which was in the following order S-600 (8.01 nm) > S-900 (7.72 nm) > S-700 (7.48 nm) > S-800 (7.05 nm). The average pore diameter decreased with increasing temperature, with S-800 exhibiting its minimum value (7.05 nm). These results demonstrate that the sample treated at 800 °C exhibited a larger specific surface area, a smaller average pore diameter than the other samples, offering an additional area for metal ion adsorption and more active sites for the catalytic reaction.

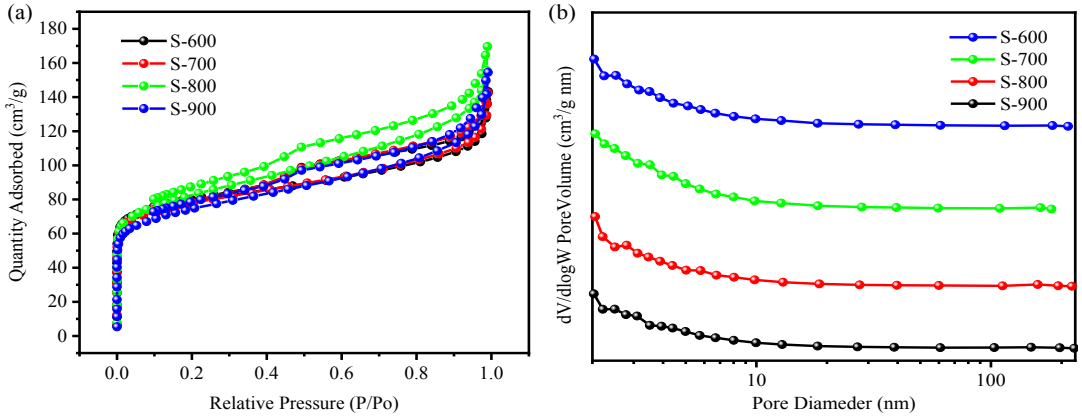

Fig. 5. (a) Nitrogen adsorption–desorption isotherms and (b) pore size distributions of the catalysts heat-treated at different temperatures.

3.2. Phase and composition analyses

XRD tests were performed on S-400, S-500, S-600, S-700, S-800, S-900 and S-1000 to determine their composition and phase characteristics (Fig. 6). It can be observed from Fig. 6 that the phase of the samples considerably changed with increasing the temperature. At a low temperature (400 °C), the samples mainly contained Fe_3O_4 (PDF 97-003-1754) diffraction peaks[23,24]. As the temperature increased to 600 °C, the Fe_3O_4 diffraction peaks disappeared and were replaced by $Ni_{0.5}Fe_{0.5}$ (PDF 04-005-8641), which had sharp and smooth diffraction peaks, indicating its good crystallinity and high purity. The diffraction peaks at 2θ = 43.9°, 51.1°, 75.1°, 91.4° and 96.7° correspond to the (1 1 1), (2 0 0), (2 2 0), (3 1 1) and (2 2 2) planes of $Ni_{0.5}Fe_{0.5}$, respectively. When the temperature was further increased to values higher than 800 °C, $Fe_9Ni_9S_{16}$ (nickel–iron–sulphide; 97-003-1754), occurred with $Ni_{0.5}Fe_{0.5}$. The diffraction peaks at 2θ = 15.2°, 29.3°, 30.7°, 46.7°, 51.2° and 71.8° corresponded to the (1 1 1), (3 1 1), (2 2 2), (5 1 1), (4 4 0) and (7 3 1) planes of $Fe_9Ni_9S_{16}$, respectively. Moreover, the grain sizes of $Ni_{0.5}Fe_{0.5}$ in the samples heat-treated at different temperatures were obtained according to the Scherrer formula [Formula (4)], and the results are listed in Table 1[26].

$$D = K\lambda/(\beta\cos\theta) \quad (4)$$

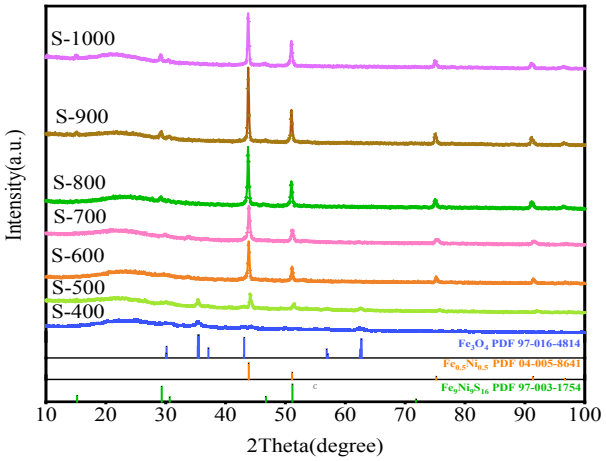

Fig. 6. XRD characterization of the samples.

Table 1. Grain size of $Ni_{0.5}Fe_{0.5}$ contained in the samples.

Sample Number	S-500	S-600	S-700	S-800	S-900	S-1000
Grain Size (nm)	27.78	28.99	25.12	30.77	34.83	30.55

Table 1 shows that the order of the grain size is as follows: S-900 > S-1000 ≈ S-800 > S-600 > S-500 > S-700. The increase in temperature increases the crystallinity of the crystal and the size of the grains.

3.3. Raman analysis

The D peak (defect peak) and G peak (graphite peak) are the characteristic Raman peaks located near 1,350 and 1,590 cm^{-1} in the Raman spectrum. The D peak is attributed to the stretching vibrations occurring at defect sites or boundaries within the material, reflecting the level of defects in the material. The G peak arises from the stretching vibration of the sp^2 hybridised C–C bonds in the carbon plane, reflecting the graphitisation degree of the material. The ratio of I_D/I_G is a common indicator to judge the graphitisation degree and crystal defect level of the material[27-29]. Figs. 7(a and b) show the Raman spectral characteristics and graphitisation degree ratio of the sample. As shown in Fig. 7a, S-500, S-600, S-700, S-800, S-900 and S-1000 exhibit clear D peaks and G peaks, indicating that the samples have different degrees of graphitisation and defect sites. Fig. 7b shows the variation of I_D/I_G value. The largest I_D/I_G value (approximately 0.91) and the highest carbon defect level were those of S-800.

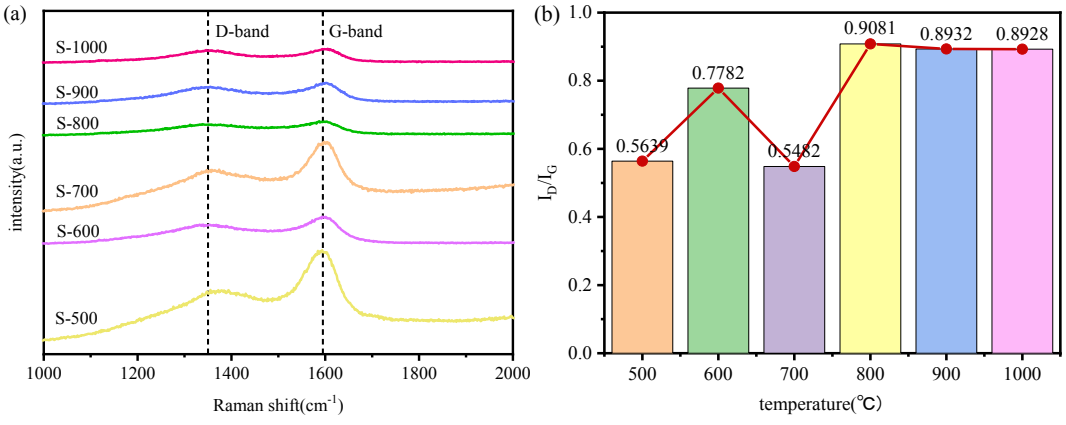

Fig. 7. (a) Raman spectra and (b) I_D/I_G of catalysts heat-treated.

This indicates that high temperature is more likely to generate defects and edges in the biomass carbon matrix, but an extremely high pyrolysis temperature (S-900 and S-1000) slightly reduces the carbon defect level.

3.4. XPS analysis

XPS spectroscopy results was show as Figs. 8(a–f). Fig. 8a show that the characteristic peaks of elements C, O, S, Ni, and Fe in all samples correspond with the EDS mapping data. The XPS spectrum of C1s, as shown in Fig. 8d, has characteristic peaks at 284.8, 286.09, and 288.8 eV, corresponding to the C-C, C-N, and C-O bonds, respectively. The C–N bond is a bond between the C and N elements contained in the biomass itself[28].

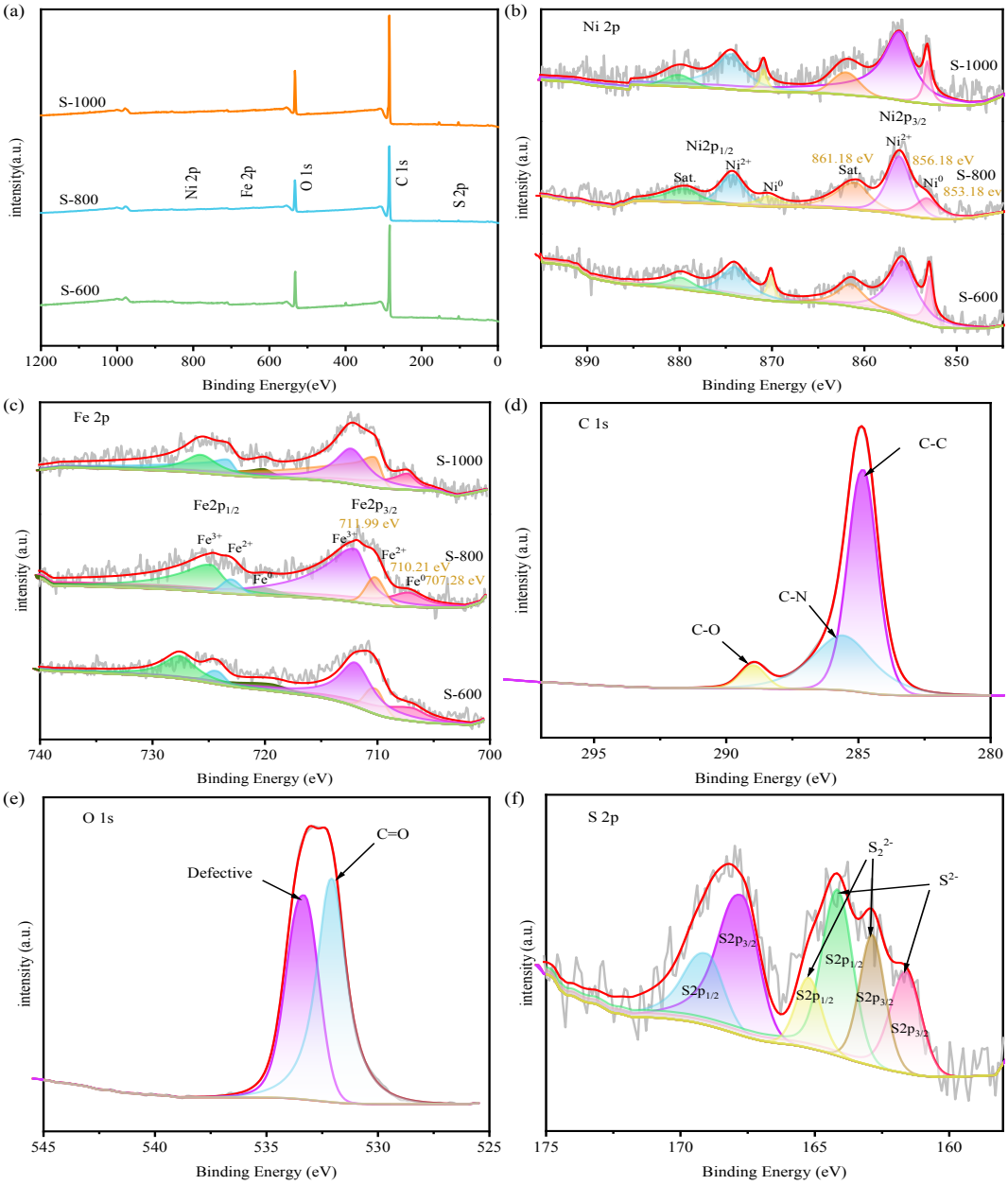

Fig. 8. (a) XPS survey spectra and high-resolution spectra of (b) Ni 2p, (c) Fe 2p, (d) C 1s (e) O 1s and (f) S 2p 1s in the NiFe–S/C.

In the Ni2p XPS spectrum shown in Fig. 8b, there are six peaks: the ones at 853.18 and 870.28 eV are indicative of Ni^0, and the peaks at 856.18 and 874.38 eV are representative of

$Ni^{2+}2p_{3/2}$ and $Ni^{2+}2p_{1/2}$, respectively[30-32]. There are also two satellite peaks at 861.18 and 879.48 eV. The XPS spectra of Fe2p (Fig. 8c) also show six peaks. The peaks at 711.99 and 724.78 eV correspond to $Fe^{3+}2p_{3/2}$ and $Fe^{3+}2p_{1/2}$, respectively. The binding energy of Fe^{2+} is low, and its peaks were observed at 710.21 and 723.08 eV. The peaks at 707.28 and 720.18 eV are attributed to Fe^{0}[33,34], respectively. XPS analysis reveals a direct proportionality between temperature and the binding energies of Ni2p and Fe2p, with the sequence being: 1,000 °C > 800 °C > 600 °C. This suggests that the temperature increase induces a strong interaction between the NiFe alloy and $(NiFe)S_x$[31]. Fig. 8e shows the O1s spectrum with two distinct peaks at 532.06 and 533.36 eV, denoting the binding energy of the C=O bond and defect O site, respectively[31,33]. Fig. 8f shows the S2p spectra with the $S2p_{3/2}$ and $S2p_{1/2}$ orbitals of S^{2-} and S_2^{2-}, which correspond to the binding energies at 161.63/164.18 and 162.88/165.23 eV, respectively. Moreover, the signals at 167.83 and 169.14 eV can be attributed to SO_4^{2-}, indicating a slight sulphur oxidation on the sample surface[30,35].

3.5. Electrochemical performance analysis

As shown in Fig. 9(a–f), the electrocatalytic activity of the catalysts prepared at 400 °C, 500 °C, 600 °C, 700 °C, 800 °C, 900 °C and 1,000 °C for OER ($4OH^- \rightarrow O_2 + 2H_2O + 4e^-$) was studied in a KOH aqueous solution (1 mol L^{-1}).

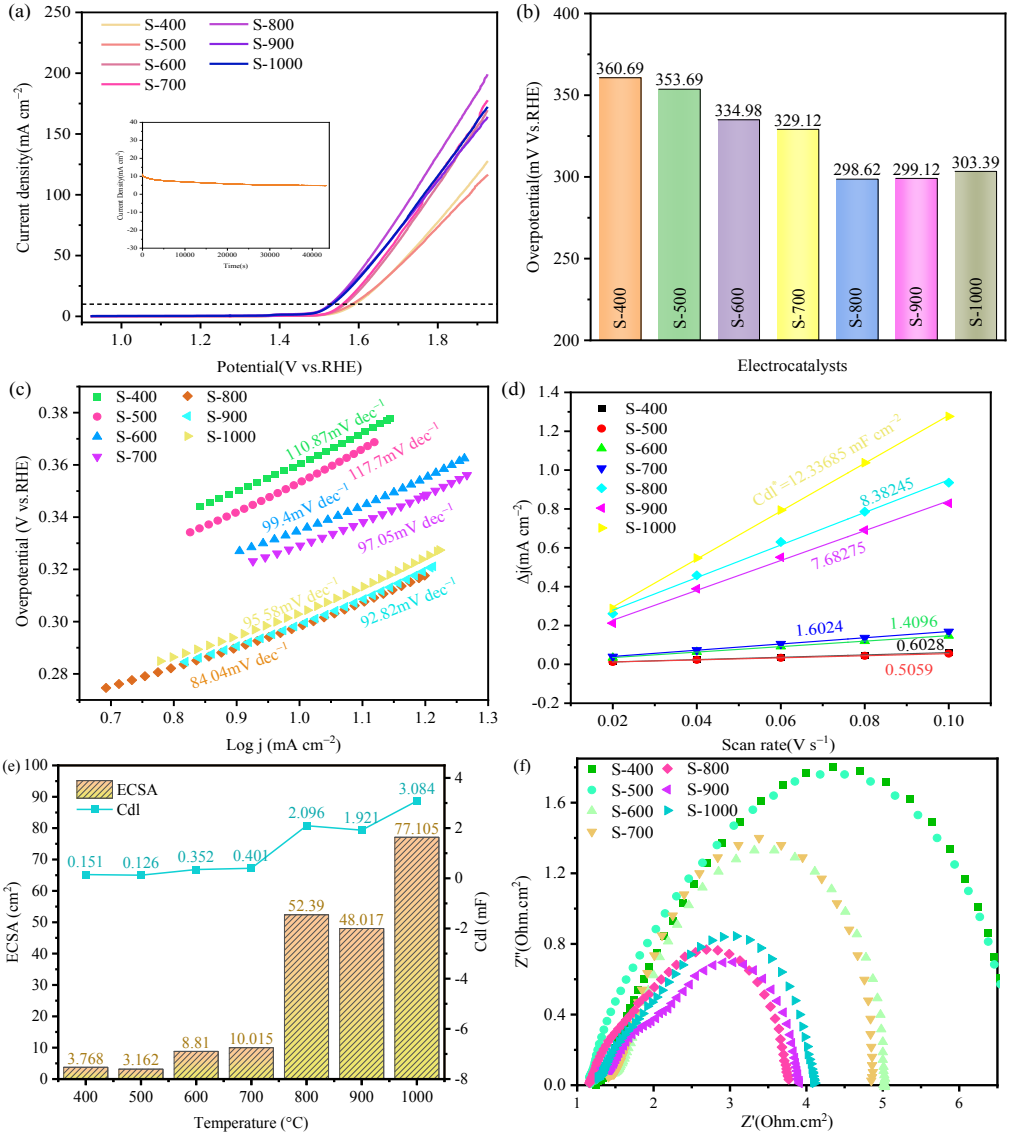

Fig. 9. (a) LSV curves, (b) overpotential at 10 mA cm^{-2}, (c) Tafel plots, (d) Cdl calculated based on the obtained CV curves. (e) Cdl and ECSA calculated based on Cdl*. (f) Nyquist plots of samples.*

Fig. 9a shows the LSV curves of the samples, indicating that S-800 exhibits the lowest overpotential. Fig. 9b depicts the overpotential bar chart of the samples, showing that S-800 exhibits overpotentials of 298.62 and 507.16 mV at 10 and 100 mA cm^{-2}, respectively, indicating its fast kinetics for OER. Fig. 9c shows the Tafel slopes of the samples, with S-900 (92.82 mV dec^{-1}), S-1000 (95.58 mV dec^{-1}), S-700 (97.05 mV dec^{-1}), S-600 (99.4 mV dec^{-1}), S-500 (117.7 mV dec^{-1}) and S-400 (110.87 mV dec^{-1}), while S-800 has the smallest at 84.04 mV dec^{-1}. As can be seen from Fig. 9f, S-800 has the smallest impedance value (3.12 Ω) and the highest conductivity. The i–t stability test indicates that S-800, which has the best OER performance, shows good stability.

The unique structure of the catalyst is the reason for its excellent OER activity. Forming a hierarchical three-dimensional channel structure requires 800 °C. The large specific surface area offers more abundant electron transfer channels for the OER process. The synthesised $Ni_{0.5}Fe_{0.5}$ enhances the synergistic effect between the two elements. The $Ni_9Fe_9S_{16}$ synthesised by doping with the S element provides more defect sites for the catalyst, facilitating the induction and positioning of OH^- and the intermediate products[36]. These two factors significantly enhance the electron transfer efficiency in the OER process, thereby improving the electrocatalytic performance.

Fig. 9d shows the Cdl* of different samples calculated based on the relationship relating to current density and scan rate. Fig. 9e presents the double layer capacitance Cdl and ECSA. The Cdl values of S-1000, S-800, S-900, S-700, S-600, S-400 and S-500 are 3.084, 2.096, 1.921, 0.401, 0.352, 0.151 and 0.126 mF, respectively. Using Formula (3), the ECSA values of S-1000, S-800, S-900, S-700, S-600, S-400 and S-500 were calculated to be 77.105, 52.39, 48.017, 10.015, 8.81, 3.768 and 3.162 cm^2, respectively. The ECSA value was relatively high at 1,000 °C but the high heat treatment temperature causes the carbon skeleton to become loose and collapse, which impairs electron transfer, consequently weakening the catalytic performance compared to that obtained at 800 °C.

The electrochemical test results are consistent with the XRD, BET, SEM and XPS tests results. The electrochemical properties of the samples can be divided into three categories, as shown by the LSV curves, ECSA and EIS. S-1000, S-900 and S-800 show analogous results. Similarly, S-700 and S-600 as well as S-500 and S-400 show similar results. There is a large gap in the overpotential, ECSA and impedance among the three categories. This may be related to the structure and phase composition of the samples. The XRD and XPS results show that the Fe_3O_4 phase mainly occurs in S-400 and S-500, in which the nickel–iron alloy phase has not been generated and thus cannot exert good catalytic activity. The $Ni_{0.5}Fe_{0.5}$ alloy crystal phase occurs in S-600 and S-700. In S-1000, S-900 and S-800, a more pronounced $Fe_9Ni_9S_{16}$ crystal phase is generated. The sulphide and nickel–iron alloy form a multi-phase concomitant mixed crystal composite. The heterojunction between the crystal phases can considerably improve the catalytic activity of the catalyst materials.

4. Conclusions

Herein, a method was designed for preparing biomass carbon materials with a porous skeleton structure and sulphur-doped NiFe-based catalysts with a flower-like structure. Sorghum husk, which is naturally abundant, was used as the raw material, achieving an efficient and comprehensive utilisation of biomass waste. The proposed method provides a cost-effective, efficient and environmentally friendly path for carbon sequestration and emission reduction within the research of green hydrogen energy.

Using an *in situ* metal salt ion solution impregnation–heat treatment technology, biomass porous carbon-supported sulphur-doped flower-like NiFe-based composite catalysts ($Ni_{0.5}Fe_{0.5}/Fe_9Ni_9S_{16}$) were successfully prepared. The prepared mixed crystal composite catalyst exhibited excellent OER catalytic performance for water decomposition. At the condition of 10 mA cm^{-2}, the overpotential was 298.62 mV and the Tafel slope was 84.04 mV dec^{-1}. Moreover, the catalyst exhibited good stability in alkaline electrolytes.

The $Ni_{0.5}Fe_{0.5}/Fe_9Ni_9S_{16}$ mixed crystal composite material exhibited excellent catalytic performance, which can mainly be attributed to three factors. (1) The three-dimensional porous structure of biomass carbon, which serves as a catalyst support, facilitates the diffusion of the substances within the solid–liquid–gas phases. (2) The spherical petal-shaped alloy has a high specific surface area and a multitude of active sites, increasing the contact area with the electrolyte. (3) Heterojunctions form between nickel and iron and between metals and sulphides. The high chemical activity at the interface promotes electron transfer, reduces overpotential as well as the surface resistance and improves conductivity.

Acknowledgements

This work was supported by Sichuan Science and Technology Program (2023YFG0229), Doctoral Fund of Chengdu University (2081919131).

References

[1] A. I. Osman, N. Mehta, A. M. Elgarahy, M. Hefny, A. Al-Hinai, A. a. H. Al-Muhtaseb, D. W. Rooney, Environmental Chemistry Letters 20(1), 153 (2021); https://doi.org/10.1007/s10311-021-01322-8

[2] Y. Xu, X. Zhang, Y. Liu, R. Wang, Y. Yang, J. Chen, Environ Sci Pollut Res Int 30(5), 11302 (2023); https://doi.org/10.1007/s11356-022-24728-5

[3] H. Li, J. Guo, Z. Li, J. Wang, Molecules 28(13), 5010 (2023); https://doi.org/10.3390/molecules28135010

[4] M. Yu, E. Budiyanto, H. Tuysuz, Angew Chem Int Ed Engl 61(1), e202103824 (2022); https://doi.org/10.1002/anie.202103824

[5] Z. Ying, L. Gao, X. Zheng, B. Dou, G. Cui, International Journal of Hydrogen Energy 47(67), 28782 (2022); https://doi.org/10.1016/j.ijhydene.2022.06.252

[6] C. Hu, L. Zhang, J. Gong, Energy & Environmental Science 12(9), 2620 (2019); https://doi.org/10.1039/C9EE01202H

[7] K. Zhang, R. Zou, Small 17(37), e2100129 (2021);https://doi.org/10.1002/smll.202100129 https://doi.org/10.1002/smll.202100129

[8] Y. Zhang, Q. Fu, B. Song, P. Xu, Accounts of Materials Research 3(10), 1088 (2022); https://doi.org/10.1021/accountsmr.2c00161

[9] Y. Feng, H. Yang, X. Wang, C. Hu, H. Jing, J. Cheng, International Journal of Hydrogen Energy 47(41), 17946 (2022); https://doi.org/10.1016/j.ijhydene.2022.03.270

[10] D. A. Corrigan, Journal of The Electrochemical Society 134(2), 377 (1987); https://doi.org/10.1149/1.2100463

[11] M. W. Louie, A. T. Bell, J Am Chem Soc 135(33), 12329 (2013); https://doi.org/10.1021/ja405351s

[12] A. Y. Ahmed, D. S. Dhawale, T. A. Kandiel, Sustainable Energy & Fuels 7(13), 3025 (2023); https://doi.org/10.1039/D3SE00527E

[13] H. Kang, H. Li, X. Zhao, L. Yang, S. Xu, Ceramics International 46(3), 2792 (2020); https://doi.org/10.1016/j.ceramint.2019.09.270

[14] W. Li, C. Wang, X. Lu, Journal of Materials Chemistry A 9(7), 3786 (2021); https://doi.org/10.1039/D0TA09495A

[15] Gong K, Du F, Xia Z, Science 323(5915), 760 (2009); https://doi.org/10.1126/science.1168049

[16] X. Guo, G.-L. Cao, F. Ding, X. Li, S. Zhen, Y.-F. Xue, Y.-M. Yan, T. Liu, K.-N. J. J. O. M. C. A. Sun, Journal of Materials Chemistry A 3(9), 5401 (2015); https://doi.org/10.1039/C5TA00087D

[17] R. Mo, S. Wang, H. Li, J. Li, S. Yang, J. Zhong, Electrochimica Acta 290, 649 (2018); https://doi.org/10.1016/j.electacta.2018.08.118

[18] C. Hu, R. Paul, Q. Dai, L. Dai, Chem Soc Rev 50(21), 11785 (2021); https://doi.org/10.1039/D1CS00219H

[19] H. Wang, J. Xu, J. Xie, C. Wang, P. Bai, Materials Chemistry and Physics 272, 125049 (2021); https://doi.org/10.1016/j.matchemphys.2021.125049

[20] C. C. Mccrory, S. Jung, J. C. Peters, T. F. Jaramillo, J Am Chem Soc 135(45), 16977 (2013); https://doi.org/10.1021/ja407115p

[21] L. Sondermann, W. Jiang, M. Shviro, A. Spiess, D. Woschko, L. Rademacher, C. Janiak, Molecules 27(4), 1241 (2022); https://doi.org/10.3390/molecules27041241

[22] K. Pan, Y. Zhai, J. Zhang, K. Yu, Materials (Basel) 12(20), 3364 (2019); https://doi.org/10.3390/ma12203364

[23] H. Yuan, X. Ma, Z. Xu, Science China Chemistry 54(1), 257 (2011); https://doi.org/10.1007/s11426-010-4185-7

[24] J. Qi, Y. Gao, S. Tang, L. Jiang, S. Yan, J. Guo, Q. Xin, G. Sun, Chinese Journal of Catalysis 27(8), 708 (2006); https://doi.org/10.1016/S1872-2067(06)60038-7

[25] R. H. Tammam, A. H. Touny, M. E. Abdesalam, M. M. Saleh, Journal of Electroanalytical Chemistry 823, 128 (2018); https://doi.org/10.1016/j.jelechem.2018.06.002

[26] S. M. Hashemnejad, M. Parvari, Chinese Journal of Catalysis 32(1-2), 273 (2011); https://doi.org/10.1016/S1872-2067(10)60175-1

[27] C. T. Selepe, S. S. Gwebu, T. Matthews, T. A. Mashola, L. L. Sikeyi, M. Zikhali, N. W. Maxakato, Nanomaterials 11(10), 2725 (2021); https://doi.org/10.3390/nano11102725

[28] J. Miao, X. Zhao, H.-Y. Hu, Z.-H. Liu, Colloids and Surfaces A: Physicochemical and Engineering Aspects 635, 128092 (2022); https://doi.org/10.1016/j.colsurfa.2021.128092

[29] K. Huang, M. Chang, J. Zhang, Z. Luo, Y. Zhang, K. Zhao, W. Wang, D. Chen, Energy Technology 11(7), 2201450 (2023); https://doi.org/10.1002/ente.202201450

[30] Q. Wu, S. Wang, J. Guo, X. Feng, H. Li, S. Lv, Y. Zhou, Z. J. N. R. Chen, (2022); https://doi.org/10.1007/s12274-021-3800-6

[31] Y. Zou, B. Xiao, J.-W. Shi, H. Hao, D. Ma, Y. Lv, G. Sun, J. Li, Y. Cheng, Electrochimica Acta 348, 136339 (2020); https://doi.org/10.1016/j.electacta.2020.136339

[32] Z. Wu, Z. Wang, F. Geng, ACS Appl Mater Interfaces 10(10), 8585 (2018); https://doi.org/10.1021/acsami.7b16953

[33] X. Bai, Y. Ma, Q. Wang, J. Guan, International Journal of Hydrogen Energy 47(4), 2304

(2022); https://doi.org/10.1016/j.ijhydene.2021.10.119

[34] S.-H. Cai, X.-N. Chen, M.-J. Huang, J.-Y. Han, Y.-W. Zhou, J.-S. Li, Journal of Materials Chemistry A 10(2), 772 (2022); https://doi.org/10.1039/D1TA08385F

[35] X. Chen, X. Wang, X. Zhang, K. Srinivas, D. Liu, X. Zhao, H. Yu, B. Wang, W. Zhang, Y. Chen, Journal of Materials Science 56(34), 19144 (2021); https://doi.org/10.1007/s10853-021-06460-6

[36] L. Tao, M. Qiao, R. Jin, Y. Li, Z. Xiao, Y. Wang, N. Zhang, C. Xie, Q. He, D. Jiang, G. Yu, Y. Li, S. Wang, Angew Chem Int Ed Engl 58(4), 1019 (2019); https://doi.org/10.1002/anie.201810207